

A Deep, Wide-Field Study of Holmberg II with Suprime-Cam: Evidence for Ram Pressure Stripping^{*}

Edouard J. Bernard,¹† Annette M. N. Ferguson,¹ Michael K. Barker,¹
 Michael J. Irwin,² Pascale Jablonka,^{3,4} Nobuo Arimoto^{5,6}

¹SUPA, Institute for Astronomy, University of Edinburgh, Royal Observatory, Blackford Hill, Edinburgh EH9 3HJ

²Institute of Astronomy, Cambridge University, Cambridge CB3 0HA

³Laboratoire d’Astrophysique, Ecole Polytechnique Fédérale de Lausanne (EPFL), Observatoire, CH-1290 Sauverny, Switzerland

⁴GEPI, Observatoire de Paris, CNRS UMR 8111, Université Paris Diderot, F-92125 Meudon Cedex, France

⁵Subaru Telescope, 650 North A’ohoku Place, Hilo, Hawaii 96720, U.S.A.

⁶Graduate University for Advanced Studies, 2-21-1 Osawa, Mitaka, Tokyo 181-8588, Japan

Accepted ?. Received 2012 August 23; in original form 2012 July 25

ABSTRACT

We present a deep, wide-field optical study of the M81 group dwarf galaxy Holmberg II (HoII) based on Subaru/Suprime-Cam imaging. Individual stars are resolved down to $I \sim 25.2$, i.e. about 1.5 mag below the tip of the red giant branch (RGB). We use resolved star counts in the outskirts of the galaxy to measure the radial surface brightness profile down to $\mu_V \sim 32$ mag arcsec $^{-2}$, from which we determine a projected exponential scalelength of $0.70' \pm 0.01'$ (i.e. 0.69 ± 0.01 kpc). The composite profile, ranging from the cored centre out to $R=7'$, is best fit by an EFF profile which gives a half-light radius of $1.41' \pm 0.04'$ (i.e. 1.39 ± 0.04 kpc), and an absolute magnitude $M_V = -16.3$. The low surface-brightness stellar component of HoII is regular and symmetric and has an extent much smaller than the vast H α cloud in which it is embedded. We compare the spatial distribution of the young, intermediate age, and old stellar populations, and find that the old RGB stars are significantly more centrally concentrated than the young stellar populations, contrary to what is observed in most dwarf galaxies of the Local Universe. We discuss these properties in the context of the comet-like distribution of H α gas around HoII, and argue for the presence of a hot intragroup medium in the vicinity of HoII to explain the contrasting morphologies of the gas and stars.

Key words: galaxies: individual: Holmberg II – galaxies: dwarf – galaxies: irregular – galaxies: stellar content – galaxies: groups: individual: M81 group – intergalactic medium.

1 INTRODUCTION

In spite of their intrinsic faintness and minimal contribution to the total light, the stellar outskirts of galaxies hold crucial information about the processes of galaxy formation and evolution. Interactions, mergers and accretions all leave their imprint on the outer stellar populations in the form of substructures, streams and diffuse haloes. In addition, the long evolutionary timescales and high sensitivity to external influences means that coherent substructures are easier to detect and longer-lived than in the denser inner regions.

Considerable effort has been devoted to studying the

outer regions of massive galaxies (see, e.g. Barker et al. 2012, and references therein) which, according to hierarchical models of galaxy formation, have acquired a significant fraction of their mass through mergers and accretion episodes. The stellar peripheries of low mass dwarf galaxies have been much less studied. Most work to date has focused on Local Group (LG) galaxies (e.g. Fornax: Coleman et al. 2005; NGC6822: de Blok & Walter 2006; Sculptor: Westfall et al. 2006), although a few dwarfs in nearby groups have also been targeted (e.g. Ryś et al. 2011). The strong morphology-density relation exhibited by dwarf galaxies suggests external mechanisms play a major role in shaping their evolution (e.g. Weisz et al. 2011); surveying their stellar outskirts may therefore yield clues on the dominant processes involved.

^{*} Based on data collected at Subaru Telescope, which is operated by the National Astronomical Observatory of Japan.

† E-mail: ejb@roe.ac.uk

The global picture emerging from previous work is that most dwarf galaxies have a smooth, and generally old and

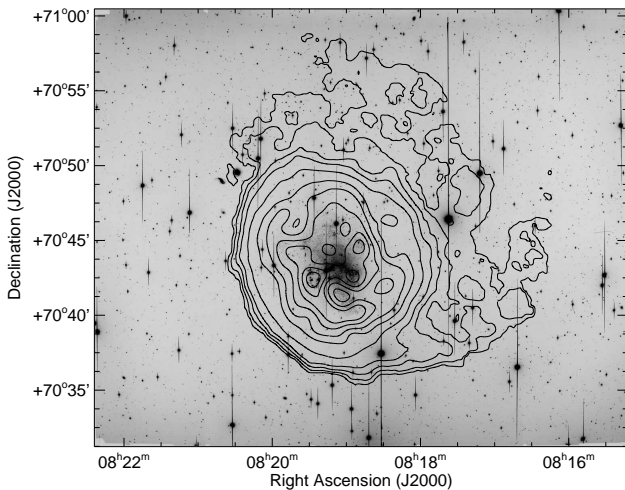


Figure 1. Mosaic V image of HoII, showing the whole field-of-view of our Subaru data ($\sim 35.8' \times 29.3'$). The H_I contours from BC02, ranging from $N_{HI} = 0.1$ to 19×10^{20} atoms cm⁻², are overplotted. Note the comet-like morphology of the outermost contour.

metal-poor ‘halo’ surrounding a more concentrated, younger and/or more metal-rich population. While the stellar haloes of large galaxies are believed to have formed from the accretion of smaller galaxies at high redshift, it is unclear whether this process has been significant in dwarfs. For example, pure accretion cannot explain the main properties of dwarf galaxies’ haloes, i.e., smooth distribution, and the existence of age and/or metallicity gradients. Instead, these observations suggest either a ‘shrinking’ scenario, in which the region of active star formation contracts as gas supply diminishes (Hidalgo et al. 2009; Zhang et al. 2012), or radial migration of stars formed close to the centre towards the outskirts (Stinson et al. 2009).

Here we analyse the stellar outskirts of the dwarf galaxy Holmberg II (hereafter abbreviated as HoII). HoII is a dwarf irregular galaxy in the M81 group that was discovered by Holmberg (1950) while surveying the galaxies in this group. Due to its location on the near-side of the group (($m-M$)₀=27.65, i.e. 3.4 Mpc), as well as its proximity to the Sc spiral galaxy NGC2403 and similar radial velocity, it is usually associated with the NGC2403 subgroup along with three other dwarf irregular galaxies (Karachentsev et al. 2002). HoII is very similar to the Small Magellanic Cloud (SMC) in terms of absolute magnitude, H_I and total mass: $M_B \sim -16.7$, $M_{HI} \sim 6 \times 10^8 M_\odot$, and $M_{tot} = 2.1 \times 10^9 M_\odot$ (Walter et al. 2007; Oh et al. 2011) compared to $M_B \sim -16.1$, $M_{HI} \sim 4 \times 10^8 M_\odot$, and $M_{tot} = 2.4 \times 10^9 M_\odot$ for the SMC (Stanimirović et al. 1999; Stanimirović, Staveley-Smith, & Jones 2004).

While HoII has been observed at all wavelengths, to date the only deep resolved stellar populations study comes from HST/ACS observations (Weisz et al. 2009) which cover a relatively small fraction of the galaxy. The need for deep wider data is especially motivated by the striking morphology of its H_I cloud. From deep VLA data, Bureau & Carignan (2002, hereafter BC02) found that the distribution of neutral hydrogen has a cometary appearance – compressed on one side with a faint extended component

on the opposite side – with the tail pointing away from the centre of the M81 group. BC02 argued that HoII is moving toward the M81 group and that ram pressure from a hot intragroup medium (IGM) is responsible for the H_I morphology, although they could not rule out the alternative interpretation of a gravitational interaction between HoII and one of its fainter neighbours.

Possible signatures of ram pressure stripping have been observed in a number of galaxies of the local universe (e.g. Condon 1983; Gavazzi et al. 1995; Ryder et al. 1997; Kenney, van Gorkom, & Vollmer 2004; Chung et al. 2007; McConnachie et al. 2007). However, most of these galaxies are too distant to be resolved into individual stars and their analyses have been confined to fairly high surface brightness inner regions. Knowledge of the distribution of resolved stellar populations at very large radii is fundamental because the stars do not respond to ram pressure. On the other hand, tidal forces affect gas and stars equally so both components should exhibit similar asymmetries. Comparing the large-scale distribution of the stars with that of the gas in HoII has the potential to reveal whether the H_I morphology was caused by ram pressure, tidal forces, or a combination of both.

In this paper we present a deep, wide-field study of HoII based on Subaru/SuprimeCam data, and analyse the properties of its stellar populations in the context of the comet-like shape of the H_I cloud in which it is embedded. In Section 2, we describe the observations and data reduction, and present the resulting CMDs in Section 3. The spatial distribution of the various stellar populations are described in Section 4. In Section 5, we present the radial profile and constrain the spatial extent of HoII. We discuss the implications of our results regarding the peculiar stellar and H_I distributions in Section 6, and summarize the main results in Section 7.

2 OBSERVATIONS AND DATA REDUCTION

2.1 Observations and Image Processing

The observations of HoII (=UGC 4305 =DDO 50 =Arp 268) were obtained in service mode with the Suprime-Cam instrument (Miyazaki et al. 2002) on the 8-m Subaru telescope (P.I.: M. Barker). The data were acquired on the night of December 18, 2009. Suprime-Cam is a mosaic camera made of 10 chips disposed in two rows of five chips – thus producing 10 images per exposure – leading to a large field-of-view (FOV; $34' \times 27'$). A single pointing was therefore sufficient to cover the relatively small galaxy ($R_{25} = 4.1'$; from HYPERLEDA: Paturel et al. 2003), including the large H_I cloud in which it is embedded ($R \sim 16'$; BC02). This is illustrated in Figure 1, showing the V-band mosaic from our Subaru data where the H_I contours from BC02 have been overlaid.

Ten exposures were obtained in each band, with individual exposure times of 600s in Johnson *V* and 240s in Cousin *I*. A small dithering pattern was used to cover the gaps between the chips as well as limit the effects of bad pixels and other camera defects, resulting in a mosaic image of $\sim 35.8' \times 29.3'$. The observations were carried out in photometric conditions, with seeing in the range $0.65 - 0.95''$. However, due to HoII’s location at high declination, it can



Figure 2. Color composite mosaic of HoII from our Subaru data. The image is cropped to $\sim 14'$ on a side; North is up and East to the left.

only be observed at relatively large airmasses from Hawaii ($\gtrsim 1.6$), so the median seeing measured in the V and I images is 0.96 and 0.76'', respectively.

The image processing procedures were similar to those followed by Barker et al. (2009, 2012). After converting each exposure to a single multi-extension FITS file, all images and calibration frames were run through a variant of the data reduction pipeline developed for processing Wide Field Camera (WFC) data from the Isaac Newton Telescope (INT) – for further details see Irwin (1985, 1997); Irwin & Lewis (2001); Irwin et al. (2004).

First stage image processing steps included bias and overscan-correction, together with trimming to the reliable active detector area. Master flats were created by stacking a dithered set of 10 V and 12 I twilight sky exposures. The flat-fielding step also corrects for internal gain variations between the detectors. After flat-fielding the dark sky I -band images were examined for signs of fringing, but as for other similar Subaru data, this was found to be negligible.

Prior to stacking, detector-level catalogues were generated for each individual processed science image to refine the astrometric calibration and also to assess the data quality. For astrometric calibration, a Zenithal polynomial projection (Greisen & Calabretta 2002) was used to define the World Coordinate System (WCS). A fifth-order polynomial includes all the significant telescope radial field distortions leaving just a six-parameter linear model per detector to completely define the required astrometric transformations. The Two Micron All Sky Survey (2MASS) point-source catalogue (Cutri et al. 2003) was used for the astrometric reference system.

During the stacking process the individual Subaru catalogues were used in addition to the standard WCS solution, to further refine to the sub-pixel level the alignment of the component images. The common background regions in the overlap area from each image in the stack were used to compensate for sky variations during the exposure sequence

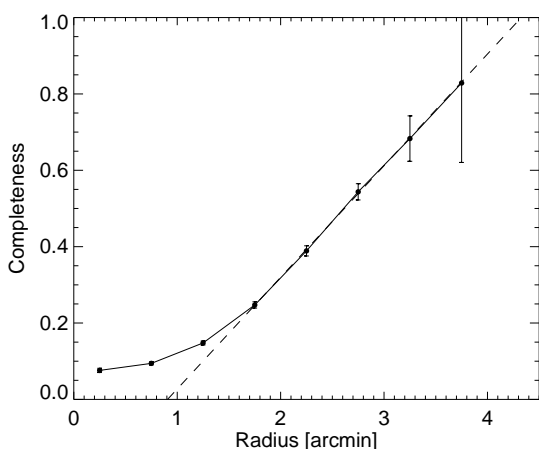


Figure 3. Completeness of the Subaru data, relative to the HST/ACS data, as a function of galactocentric radius for stars brighter than $I_0=24.5$. The dashed lines is a fit to the points between $R=1.5$ and $4'$.

and the final stack included seeing weighting, confidence (i.e. variance) map weighting and clipping of cosmic rays.

As a final image processing step, catalogues were derived from the deep stacks for each detector and their WCS astrometry was updated prior to forming the mosaic over all detectors. Any residual small offsets in the underlying sky level between each detector stack were removed iteratively by visual inspection of a 4×4 blocked mosaic of the whole field.

Full resolution mosaics were used to provide an initial set of full-field catalogues based on standard aperture photometry (e.g. Irwin et al. 2004). Since no standard star field was observed, we used INT WFC V - and i -band observations centred on H α II and taken in photometric conditions during April 2009 to derive the photometric calibration for the mosaics. The INT WFC V, i photometry was first converted to the Johnson-Cousins system (e.g. McConnachie et al. 2003) and then directly used to calibrate the Subaru data with an estimated systematic error of ± 2 per cent.

Figure 2 shows a colour composite image obtained from the V and I mosaics, which highlights the irregular morphology and strong contribution from the young, blue supergiant stars.

2.2 Profile-fitting Photometry

Given the very high stellar density in H α II, we subsequently decided to perform profile-fitting photometry which is better suited to obtain accurate measurements in crowded fields. The PSF photometry was carried out with the DAOPHOT/ALLSTAR/ALLFRAME suite of programs (Stetson 1994) as follows. We performed a first source detection at the 3σ level on the individual images, which was used as input for aperture photometry. From these catalogues, 300 bright, non-saturated stars per image were initially selected as potential PSF stars. An automatic rejection based on the shape parameters was used to clean the lists, followed by a visual inspection of all the stars to remove the remaining unreliable stars. We ended up with clean lists containing at

least 150 good PSF stars per image. Modelling of the empirical PSF with a radius of 12 pixels was done iteratively with DAOPHOT: the clean lists were used to remove all the stars from the images except PSF stars, so that accurate PSFs could be created from non-crowded stars. At each iteration, the PSF was modelled more accurately and thus the neighbouring stars removed better. Every 3 to 5 iterations, the degree of PSF variability across the image was also increased, from constant to linear, then quadratically variable.

The following step consisted of profile-fitting photometry on the individual images using ALLSTAR with the empirical PSFs previously created. The resulting catalogues were matched on a chip-by-chip basis, keeping only the objects for which the PSF fitting converged in at least three images per band to limit the number of false detections, to create one clean stellar catalogue per chip. These catalogues were further cleaned by rejecting extended objects based on the sharpness parameter, then merged to produce a master catalogue for the whole Suprime-Cam FOV. This catalogue was then used as the input star list for ALLFRAME, which was run on all the individual images at once. The output of ALLFRAME consists of a catalogue of PSF photometry for each individual image. A robust mean magnitude was obtained for each star by matching these catalogues.

The final photometry was calibrated to the Johnson-Cousin standard system by matching ~ 1750 bright stars in common with the calibrated aperture photometry described in the previous Section. The uncertainty on the offset between the aperture and PSF photometry is smaller than 0.001 in both bands and therefore represents a negligible contribution to the total magnitude uncertainties.

According to the Schlegel, Finkbeiner, & Davis (1998) reddening maps, the area covered by our observations suffers from minor foreground differential reddening, with $E(B-V)$ ranging from about 0.023 to 0.033. To obtain accurate photometry over the whole FOV, each individual star was corrected for reddening based on its location. We note that the corresponding dust mask map indicates that a small area centred on H α II (out to $r\sim 6'$; i.e. ~ 10 per cent of the Subaru FOV), as an extragalactic source, was removed from the dust map and replaced with the median value of the surrounding pixels. This means that the star-by-star correction does not include extinction internal to H α II.

Finally, the astrometric calibration for the whole stellar catalogue was obtained with the IRAF tasks *ccxymatch*, *cemap*, and *cctrans* using ~ 800 stars in common with Version 2.3.2 of the Guide Star Catalog II (Lasker et al. 2008). The accuracy of the resulting astrometry is about $0.3''$.

2.3 Completeness

To estimate the completeness of our data, we retrieved the HST/ACS photometry of H α II from the ACS Nearby Galaxy Survey Treasury program (ANGST; Dalcanton et al. 2009). While it only covers a tiny fraction of our FOV (~ 2 per cent), it is located on the highest density area which is the most affected by incompleteness. It is ~ 3 mag deeper than our Subaru photometry and much less affected by stellar crowding thanks to the higher spatial resolution of the instrument. Therefore, in the following we assume that it is 100 per cent complete in the range of magnitudes covered

by our Subaru data, and representative of the intrinsic photometric properties of the stars in HoII.

We used DAOMATCH and DAOMASTER (Stetson 1993) to match the HST and Subaru photometric catalogues. These programs are based on the robust ‘matching triangles’ technique, rather than assuming a given matching radius. This ensures a proper matching of the stars even in very crowded regions, regardless of the possible translations, rotations, scale changes, or flips of the coordinate systems.

Using all the stars from the area in common between the two photometric catalogues, we find the 50 per cent completeness limits of the Subaru data at $V_0=23.93$ and $I_0=23.00$. However, the centre of the galaxy is more affected by crowding than the outer regions, so completeness varies significantly with radius. To correct the radial density profile shown in Section 5, which uses all the stars with $I_0 < 24.5$, we therefore estimate the completeness down to this magnitude as a function of radius. The result is shown in Figure 3. For each annulus, the errorbar was calculated by adding in quadrature the Poisson uncertainties on the number of stars in the HST and Subaru subsamples. We find that completeness varies from 10 per cent in the inner $0.5'$ to 90 per cent at $R\sim 4'$. The dashed line is a fit to the points between $R=1.5$ and $4'$, and suggests that we can assume ~ 100 per cent completeness beyond $4'$.

3 COLOUR-MAGNITUDE DIAGRAMS

The resulting colour-magnitude diagrams (CMDs) for the field and HoII stars are shown in Figure 4. We used the 0.1 and 2×10^{20} atoms cm^{-2} H I contours to separate the two populations (see Section 4): stars outside the former are assumed to be field stars while stars inside the latter are considered HoII. The CMDs were cleaned of non-stellar objects using the photometric parameters given by ALLFRAME, namely $\sigma_{V,I} \leq 0.2$ and $|\text{SHARP}| \leq 1$. To enhance the features at faint magnitudes, the CMD of the top left panel was further cleaned using tighter constraints on the sharpness ($|\text{SHARP}| \leq 0.5$) but is shown only for illustrative purpose. It contains $\sim 16,600$ stars, instead of the $\sim 27,100$ stars in the CMD of the top right panel.

At I_0 brighter than ~ 22 the field CMD, shown in the bottom right panel of Figure 4, harbors two prominent vertical sequences: the main-sequence turn-off stars of the Milky Way (MW) halo at $(V-I)_0 \sim 0.7$, and dwarf stars in the MW disc at $(V-I)_0 \sim 2.5$. At fainter magnitudes, these sequences are overwhelmed by the contribution of unresolved background galaxies. We note, however, that the HoII CMDs in the top panels correspond to an area about 10 times smaller than that covered by the field stars, so the effect of the contamination by foreground stars and background galaxies is not as significant. To illustrate this, the bottom left panel shows the CMD of a field with the same area as HoII. The scaled field CMD contains ~ 7600 objects.

To help identify the features in the HoII CMDs, in the top right panel of Figure 4 we overplot isochrones from the Padua stellar evolution library (Marigo et al. 2008), shifted to the distance of HoII. The young isochrones have $Z=0.002$ and ages of 10, 20, 50, 100, and 160 Myr from top to bottom, while the old ones shown in red are 12.5 Gyr old with $Z=0.0001, 0.0003, 0.001$, and 0.002 from left to right.

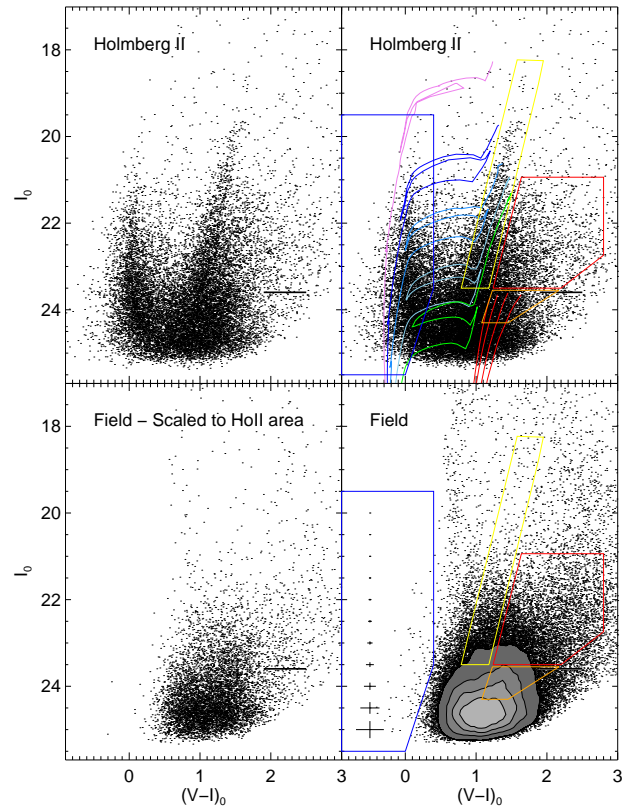


Figure 4. Extinction-corrected color-magnitude diagrams of HoII (top panels) and field stars (bottom panels). In the bottom right panel, the contour levels correspond to $[6, 12, 18, 24, 30] \times 10^3$ stars mag^{-2} , and the error bars show the mean photometric errors as a function of magnitude for both field and HoII stars. The boxes used to select the various stellar populations are shown in the right panels: MS+BSG (blue), RSG (yellow), AGB (red), and RGB (orange). Selected isochrones from the Padua library (Marigo et al. 2008) have been overplotted in the top right panel (see text for details).

The most prominent features of the HoII CMD are the blue and red supergiant branches (BSG and RSG, respectively) of core helium-burning stars at $(V-I)_0 \sim 0$ and 1.2 , respectively. Their presence indicates vigorous star formation in the past ~ 160 Myr. The BSG branch curves toward the red below $I_0 \sim 24$, and joins the RSG close to the red clump just below our limiting magnitude. Redward of the RSG and at $I_0 \gtrsim 23.5$, a higher density of stars corresponding to the red giant branch (RGB) is visible. The expected magnitude of the tip of the RGB (TRGB), from Karachentsev et al. (2002), is shown as a thin line at $I_0 = 23.60$. Some of the stars brighter than the TRGB and redder than the RSG are genuine asymptotic giant branch (AGB) stars (see Section 4), although they are difficult to separate from the contamination of foreground stars and unresolved galaxies. Finally, a few dozen main sequence (MS) stars forming a diffuse band blueward of the BSG branch are visible at about $(V-I)_0 = -0.2$ and $I_0 \gtrsim 21.5$, indicating star formation within the last 10 Myr. We note that while some of these stars lie blueward of the youngest isochrones, their concentration close to the centre of HoII confirms that they are bona fide members of HoII. Their

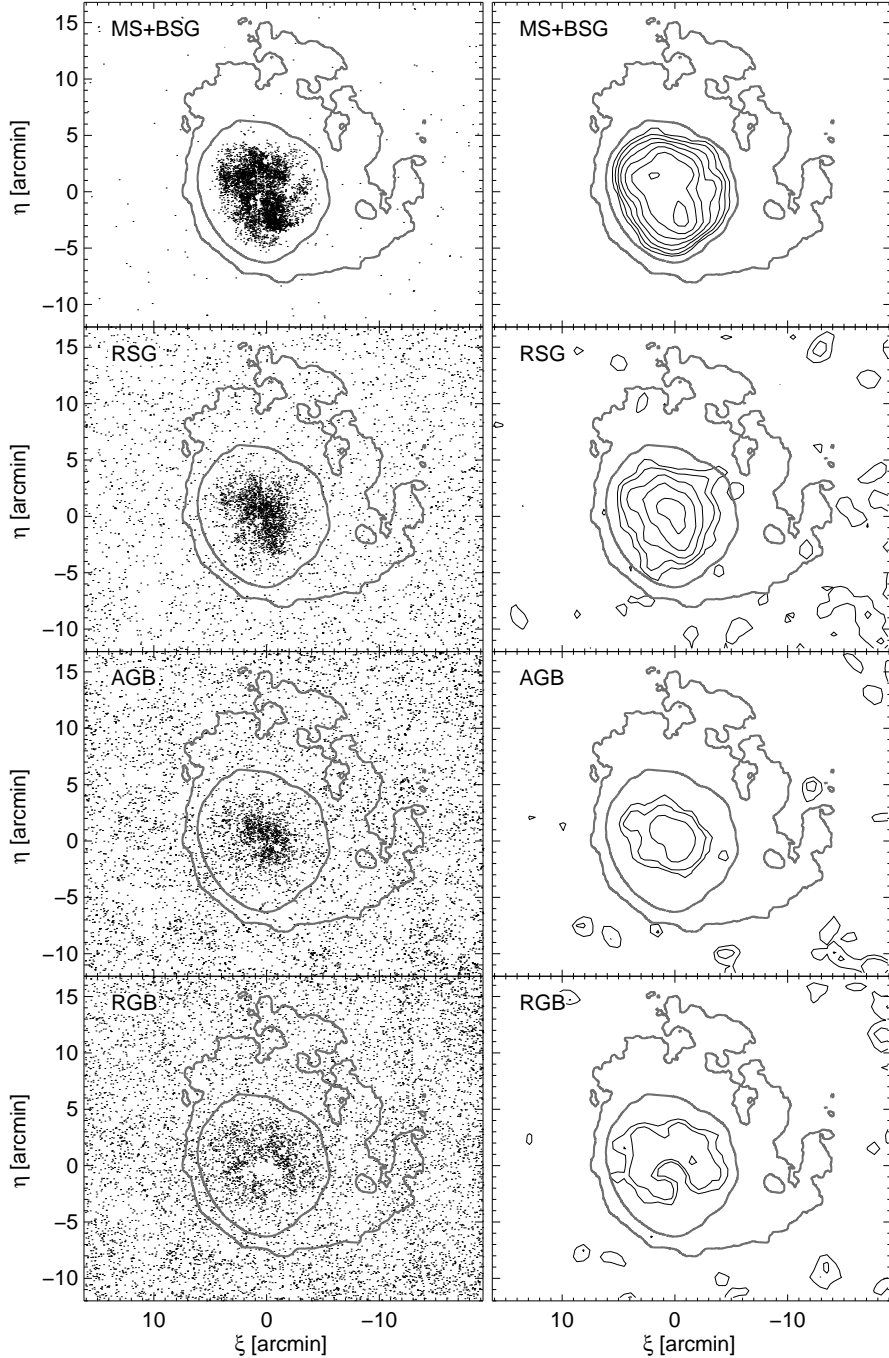


Figure 5. Spatial distribution of candidate MS+BSG, RSG, AGB and RGB stars in the whole Subaru FOV (left), and the corresponding contours (right). Stellar contours levels are arbitrary. The two H I contours (0.1 and 2×10^{20} atoms cm^{-2} , from BC02) used to separate HII and field stars are shown as thick gray lines to use as guides.

color spread, larger than expected from photometric errors only, is a consequence of the crowding in this region.

In the following Section, we analyse the spatial distributions of the different stellar populations individually. They are selected on the CMDs using the boxes shown in the right panels of Figure 4. The blue, yellow, red, and orange boxes enclose the stars belonging to the MS+BSG ($\lesssim 160$ Myr), RSG (10–160 Myr), AGB (a few hundred Myr to a few Gyr), and RGB ($\gtrsim 1.5$ Gyr), respectively. For the MS+BSG selec-

tion, we chose to use the whole range of luminosity since contamination by foreground and background sources is virtually non-existent in this color range.

4 SPATIAL DISTRIBUTION

In Figure 5 we show the spatial distribution of each individual stellar populations – selected using the boxes shown in the left panels of Figure 4 – and the corresponding contours.

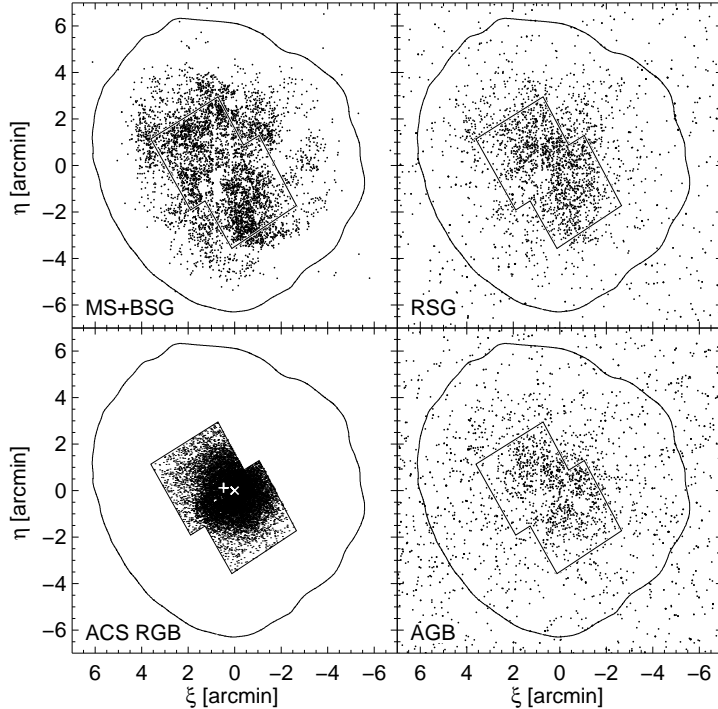


Figure 6. Zoomed-in spatial distribution of BSG, RSG, and AGB stars in the Subaru FOV, and RGB from HST/ACS data. Several small holes in the stellar distributions are due to highly saturated stars and their associated bleed spikes. The inner H₁ contour of Figure 5, as well as the outline of the combined footprint of the two ACS pointings, are shown. The cross and plus symbol in the bottom left panels represent the dynamical centre and the centre of the H₁ contour, respectively, to highlight the offset between the two.

From top to bottom, the panels show the distribution of the MS+BSG, RSG, AGB, and RGB. To serve as guides, in each panel we also plotted two H₁ contours from the BC02 study, representing densities of 0.1 and 2×10^{20} atoms cm⁻²: the first one is their lowest density contour, while the second is the innermost contour that includes most of the observed MS+BSG stars belonging to HoII. We find that the shape of the latter contour is close to an ellipse with radius $R=6.0'$, $b/a=0.90$, and position angle of 27° . These are the contours we used to separate HoII and field stars (see Section 3).

The top panels show that blue stars younger than about 160 Myr old are confined to regions where the H₁ density is higher than about 2×10^{20} atoms cm⁻². The very few objects outside the contours are distributed uniformly over the FOV, suggesting that they are either unresolved galaxies with similar colors, or foreground blue HB, blue staggler, or white dwarf stars. The outermost MS+BSG contour follows very closely the inner H₁ contour, as expected if massive star formation only occurs above a certain gas density threshold. The other panels show that contamination by field stars and unresolved galaxies increases significantly at redder color and fainter magnitudes. Nevertheless, these maps do not show significant stellar concentrations outside of the central contour, which suggests that most or all of the sources outside this area are either foreground stars or unresolved galaxies.

Interestingly, in Figure 5 the concentration seems to increase from BSG to RSG stars, and from RSG to AGB stars, the populations being more compact with increasing age. The RGB stars, close to our detection limit, are

the most affected by crowding which explains the hole in the distribution at the centre of HoII. In addition, some of the stars flagged as RGB may actually be RSG or AGB stars that were shifted to the RGB box due to photometric errors. Therefore, since the RGB distribution is not clear from our Subaru data, we checked the distribution using the HST/ACS photometry of HoII described in Section 2.3. In the bottom left panel of Figure 6 we show the distribution of RGB stars in the top 1.5 mag of the RGB from the HST dataset. The MS+BSG, RSG, and AGB maps from the Subaru data are shown in the other panels. In each panel, the black line outlines the combined footprint of the two ACS pointings to facilitate comparison.

The difference between the distributions of the MS+BSG and RGB samples is striking: despite the small area covered by the HST data, it is obvious that the old, RGB stars are significantly more concentrated than the younger stars, as already noted by Bastian et al. (2011). The former are also distributed in a roughly circular distribution, whereas the latter present a very irregular distribution. Within the ACS footprint, the density of RGB stars almost vanishes close to the edges while the density of blue stars is roughly uniform. We note that the distributions of Subaru and HST/ACS blue stars are very similar in the area in common. Using only the ACS data to avoid the uncertainties due to incompleteness and different spatial coverage, we find exponential scalelengths for the MS+BSG, RSG, AGB and RGB samples of $3.1' \pm 0.5'$, $1.7' \pm 0.3'$, $0.80' \pm 0.07'$, and $0.76' \pm 0.04'$, respectively. Given the small FOV, we did not apply a background correction to these profiles.

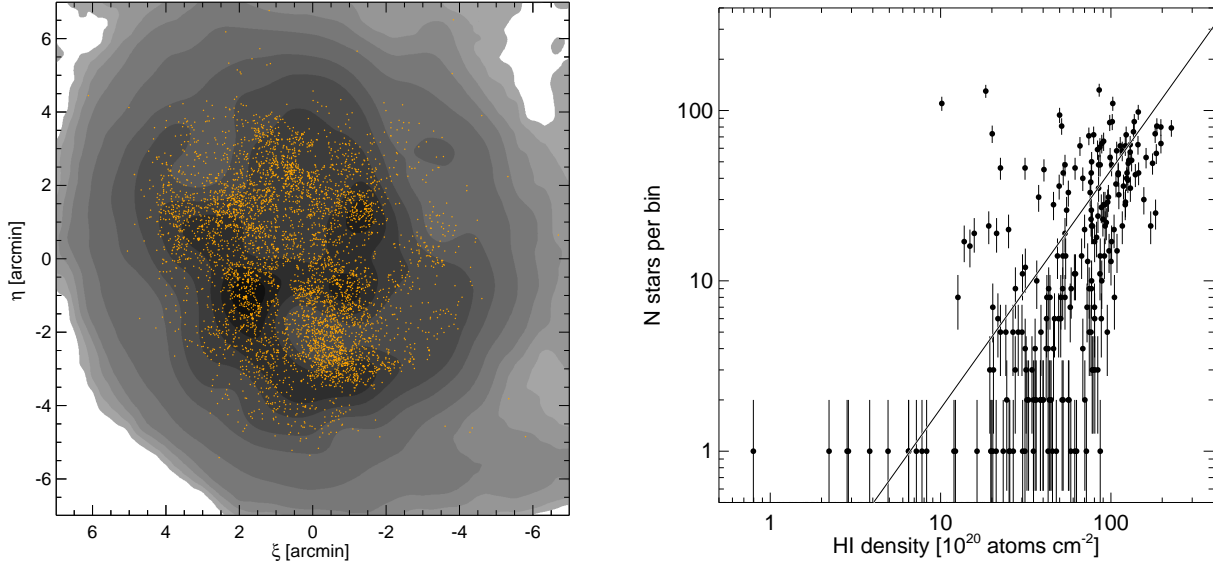


Figure 7. Left: spatial distribution of MS+BSG stars overlaid on the H₁ contours of BC02. Right: Surface density of MS+BSG stars as a function of H₁ density in square bins of 37.5'' on a side. The solid line represent the typical Kennicutt-Schmidt relation with a slope of 1.4 (Kennicutt 1998).

Figure 6 also shows that the blue stars, besides having a larger spatial extent, also seem to delineate short spiral arms. This morphology is not due to highly saturated stars or artifacts due to image defects, and completeness down to $I_0 = 24.5$ is ~ 100 per cent at large radii. These arms follow the same counter-clockwise orientation as the H₁ arms observed by Bureau et al. (2004) in the northwest of HoII, which further suggests they are real. The lack of similar arms in the distribution of AGB stars suggests these are likely transient features.

The good agreement between the distribution of young stars and the H₁ gas is further illustrated in Figure 7. The left panel presents the distribution of MS+BSG stars overlaid on the H₁ contours of BC02, and shows that these are usually located in the higher column density areas. In the right panel, we plot the number of MS+BSG stars in bins of 37.5'' on a side as a function of the H₁ density in the same bins. Note that for this panel we have used the higher resolution map of Walter et al. (2008, natural weighting, beam size $\sim 13''$) to better sample the scales of our stellar distribution. It shows that the distributions of young stars and H₁ gas are correlated. A few points at high gas density and low star counts are artifacts due to the holes left by very saturated stars and their bleed spikes. On the other hand, the datapoints with high stellar and low gas density are real: most of them are located in the main H₁ hole at $\xi \sim 0'$ and $\eta \sim -2'$, where Weisz et al. (2009) found elevated star formation about 50 Myr ago, but only low levels in the past 10–20 Myr. Interestingly, even though we use the number of MS+BSG stars (i.e. younger than about 150 Myr) as a rough proxy for the star formation rate, we find that the line representing the typical Kennicutt-Schmidt relation with a slope of 1.4 (Kennicutt 1998) provides a good match to our data.

Another interesting characteristic in Figure 6 is the apparent offset between the centres of the MS+BSG and HST/RGB star distributions, shown in the bottom left panel as the open circle and cross, respectively. We note that we applied a small shift ($\lesssim 4''$) to the astrometry of the HST data to correct for a slight mismatch between the two catalogues, so the offset is not due to inaccurate astrometry. We find that the dynamical centre listed in Stewart et al. (2000, $\alpha_{2000} = 8^h19^m05.6^s$, $\delta_{2000} = 70^\circ43'25''$) provides an excellent fit to the distribution of RGB stars. On the other hand, the centre of the inner H₁ contour, which follows very closely the distribution of MS+BSG stars, is offset from the dynamical centre by $30''$ (0.49 kpc) east and $7''$ (0.1 kpc) north. While the origin of this shift is unclear, it is reasonable to suspect that it is related to the processes that shaped the outer H₁ envelope.

5 RADIAL PROFILE

In order to obtain the radial density profile of HoII, one needs a reliable estimate of its ellipticity, position angle, and location of its centre. We use the dynamical centre described in the previous Section, which is also the centre of the intermediate-age and old stellar populations ($\gtrsim 1.5$ Gyr old). The large uncertainty on the inclination of HoII (BC02; de Blok et al. 2008; Walter et al. 2008; Oh et al. 2011; Gentile et al. 2012) prevents us from properly constraining the morphology of the galaxy. However, given the very low ellipticity of the inner H₁ contours ($1-b/a \sim 0.1$) and circular distribution of the RGB stars, we can assume circular symmetry for the purpose of calculating the radial profiles.

While resolved star counts are the optimal way to probe the very low surface brightness structure of galaxies (e.g.

Barker et al. 2009), they are not ideal at small radii due to crowding and incompleteness. As described in Section 2.3, crowding is particularly severe in the central part of HoII. However, it is possible to use diffuse light in this area and combine the contribution of both to obtain a composite profile extending over the whole radius.

For the diffuse light surface-brightness profile, we used the median pixel value in concentric circles, after masking the saturated stars and their associated bleed spikes, as well as bright background galaxies. The sky value was estimated from the mode of the pixel value distribution of the entire image. The pixel values were then converted to magnitudes per arcsec^2 , calibrated using the same zero-point as for the stellar photometry, and corrected for reddening using $E(B-V)=0.032$ (Schlegel, Finkbeiner, & Davis 1998).

The same concentric circles were used for the star count profile, in which we counted the number of stars brighter than $I_0 = 24.5$. This limit was chosen as the best compromise between sufficient number statistics and reasonable completeness correction. The background contaminant level was estimated from the density of point sources in a wide circular annulus in a region where HoII's radial profile is flat within the uncertainties ($7.5' \leq r \leq 10.5'$). For the area covered by the HST data, we applied the correction for completeness determined in Section 2.3. As for the diffuse light, the radial density profile $\Sigma(r)$ was then converted to a magnitude scale using the relation $\mu(r) = -2.5 \log \Sigma(r) + ZP$. However, here the zero-point ZP was estimated by matching the overlapping region of the stellar and diffuse light profiles ($2.5' \lesssim r \lesssim 4'$).

The resulting profiles are presented in Figure 8: the diffuse light and stellar surface-brightness profiles are shown as the gray filled circles and black filled stars, respectively. The open stars show the completeness-corrected star count profile. Although the completeness-corrected star counts and the diffuse light give reassuringly similar information in the inner regions, the star count data allow the profile to be extended to $R \sim 7'$ where $\mu_V \sim 32 \text{ mag arcsec}^{-2}$.

The surface brightness is well-described by an inner core (to $\sim 1.5'$) and a smooth outer decline. We find that an EFF (Elson, Fall, & Freeman 1987) profile provides the best description over the entire radial range, while an exponential fit also works beyond the inner core. On the other hand, the King (1962) and Plummer (1911) profiles (not shown) tend to under- and overestimate the stellar density beyond $\sim 3'$, respectively. The exponential fit to the profile between $R=1.5$ and $7'$ is shown as the dashed line, and has a scalelength of $0.70' \pm 0.01'$, or $0.69 \pm 0.01 \text{ kpc}$ at the distance of HoII. The EFF fit (solid line) leads to a half-light radius of $1.41' \pm 0.04'$ (i.e. $1.39 \pm 0.04 \text{ kpc}$) and absolute magnitude $M_V = -16.3$.

Our scalelength is slightly smaller than the estimates from Swaters ($h_B = 0.99'$ and $h_R = 0.86'$ after correcting for the difference in ellipticity; 1999). The discrepancy between the two estimates is most likely due to a combination of the shallower depth of their data ($\mu_R \lesssim 27.5$) and the steepening of our profile at larger radii. On the other hand, the radial profile of HoII shown in Oh et al. (2011) extends further out than the one presented here (out to $R \sim 9 \text{ kpc}$). We believe their extent may be overestimated as a consequence of using a relatively large ellipticity ($b/a \sim 0.66$), and a position angle determined from the $\text{H}\alpha$ data ($\text{PA}=175^\circ$) which

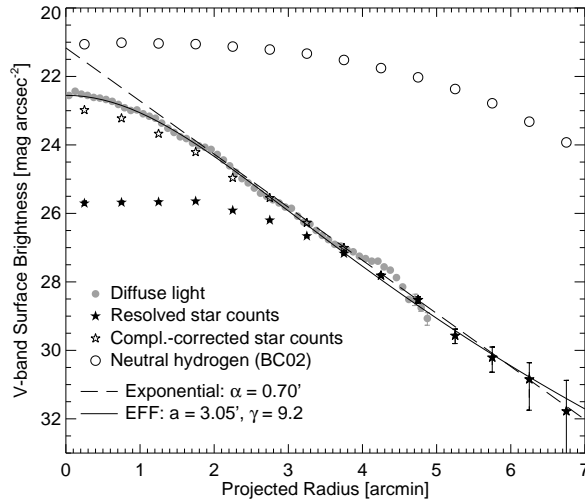


Figure 8. Background-subtracted surface brightness profiles from the diffuse light (gray filled circles), resolved star counts (filled stars), and completeness corrected star counts (open stars). The open circles represent the $\text{H}\alpha$ density profile, from BC02. The dashed and solid lines are exponential and EFF profiles fit to the composite surface brightness profile (see text).

is offset by about 35° from the position angle of the optical data ($\text{PA}=30^\circ$; Swaters 1999).

We thus find that the stellar component of HoII is significantly more compact than the $\text{H}\alpha$ cloud in which it is embedded, which extends out to $\sim 16'$ (BC02). Even if some stars belonging to HoII are present beyond $R \sim 7'$, their contribution to the galaxy luminosity is likely to be negligible. Assuming an exponential profile, such a population would represent less than 0.1 per cent of the total galaxy light.

6 DISCUSSION

6.1 Global Structure

Using the resolved stars counts in the outer regions of HoII revealed an extended structure that is an order of magnitude fainter than what can be reached with diffuse light. Outside the central $2'$ area, the profile is well-fit by an exponential model out to $R=7'$ with a scalelength of $0.69 \pm 0.01 \text{ kpc}$. However, we have also found that the scalelength is different for each stellar population, in the sense that it decreases with increasing age. This is contrary to what is usually observed in dwarf galaxies in the nearby Universe (e.g. Zhang et al. 2012), where the region of active star formation has been shrinking with time. This implies that HoII would have been a more compact galaxy in the past. The very low density of RGB stars in the outskirts of the HST fields compared to that of the younger stars can be interpreted as a significantly lower SFR in these parts $\gtrsim 1.5 \text{ Gyr}$ ago (the minimum age of stars in the top magnitude of the RGB) than in the past $\sim 160 \text{ Myr}$. This is in good agreement with the SFHs obtained from these HST data, which show a higher SFR starting about 300 Myr ago (Dalcanton et al. 2012, see also McQuinn et al. 2010), as well as a “dramatic rise in the SFR over the past 50 Myr” (Weisz et al. 2008).

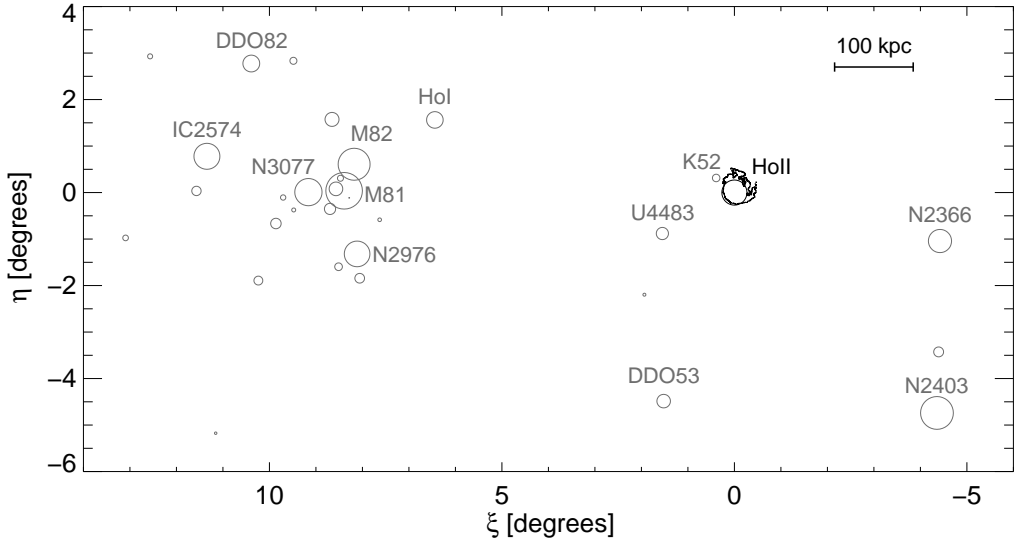


Figure 9. Distribution of galaxies in the M81 group in standard coordinates, where the symbol size is proportional to the apparent integrated B-band magnitude (Karachentsev et al. 2002). HoII is shown as the black circle at (0,0), and the main galaxies of the group are labeled. The outermost H_I contour of HoII from BC02 is also shown, scaled up in size by a factor of 2.

Given the large amount and relatively high density of the neutral hydrogen surrounding HoII (BC02), it is somewhat surprising that star formation was not more vigorous prior to about 300 Myr. This could suggest that the extended H_I has recently been acquired or that it previously had too low a density for star formation to be significant. The process that shaped the spectacular H_I envelope could have also increased the gas pressure in the inner regions of the galaxy and triggered the large scale star formation that we observe today. Two potential mechanisms to explain this are ram pressure by a hot IGM and a tidal interaction with a companion galaxy, which we discuss and compare below.

6.2 Origin of the H_I morphology?

HoII is embedded in a massive H_I cloud that is significantly more extended than the optical counterpart. The remarkable morphology of the cloud in the low density outskirts, compressed on one side with a cometary appearance on the opposite side (see Figure 1), is very suggestive of ram pressure stripping due to the presence of a hot IGM. While there are no X-ray observations to date confirming the presence of diffuse hot gas in the vicinity of HoII, such observations are available for other much smaller, ‘poor’ groups (e.g. Zabludoff & Mulchaey 1998) in which the hot IGM density can be as high as $\sim 5 \times 10^{-4}$ atoms cm⁻³ (Mulchaey et al. 1993; Sun 2012), i.e. about two orders of magnitude higher than the minimum IGM density necessary to strip the interstellar medium (ISM) of a low mass dwarf galaxy like HoII (e.g. BC02; McConnachie et al. 2007).

However, the disturbed appearance of the gas cloud may also be the result of gravitational interactions. While HoII is relatively isolated from the massive galaxies of the M81 group (see Figure 9), it has at least two companion dwarf galaxies within a projected distance of ~ 100 kpc which may have tidally affected the neutral hydrogen cloud. BC02 discussed the possible origins of the H_I morphology and con-

cluded that the ram pressure and tidal interaction scenarios were both plausible given the available information. Their follow-up study, despite the significant improvement in both coverage and sensitivity, was not sufficient to rule-out one or the other scenario (Bureau et al. 2004). They suggested that deep stellar photometry could resolve the issue by revealing a stellar counterpart to the northwest H_I structure, since ram pressure is not expected to have an effect on stars. Here we summarize the current arguments in favor of each scenario and discuss whether our deep photometry may help elucidate which is the main mechanism at play.

The deeper H_I observations of Bureau et al. (2004) revealed that the low surface brightness component in the northwest of HoII can be resolved in two or three arms, which are often associated with tidal interaction events (e.g. Dobbs et al. 2010). As shown in Section 4, the MS+BSG star distribution appears slightly distorted too, with spiral arm-like features south and west of HoII. The stellar arms also follow the same counter-clockwise orientation as the H_I arms. However, Bureau et al. (2004) also noted that the arm kinematics followed the regular rotation of the inner gas, contrary to what would be expected if they were torn from the main body by tidal interactions. In addition, while the young stars do seem to trace spiral arms, the older populations have a much more regular circular distribution. Tidal forces would affect all populations equally and the resulting stellar arms and/or tails would be made of stars of all ages. This suggests that most of the recent SF occurred in the denser H_I arms, resulting in a similar arm-like distribution of the young stars, rather than stellar tails due to tidal forces. The H_I arms, in turn, could be the consequence of ram pressure, as models which include gas cooling have shown that it can produce spiral arms (e.g. Schulz & Struck 2001; Vollmer 2003; Mapelli, Moore, & Bland-Hawthorn 2008).

Further insight comes from the detailed SFHs of HoII by Weisz et al. (2008) and Dalcanton et al. (2012), which re-

veal a significant enhancement in the last few hundred million years. Could this enhancement also be a consequence of the process that led to the striking morphology of the H_I cloud? Strong bursts of star formation are often caused by an external trigger such as an accretion event or interaction with a nearby galaxy (e.g. Kennicutt et al. 1987; Bernard et al. 2012; Cignoni et al. 2012). Indeed, as shown in Figure 9, HoII has two close companion dwarf galaxies: M81dwA (=Kar52) located at a projected distance of ~ 30 kpc to the North East, and UGC4483, ~ 110 kpc to the South East). The former, in particular, is sufficiently close that the timescale of a past interaction is roughly compatible with the enhanced SFR found by Dalcanton et al. (2012). Assuming a relative velocity of 100 km s⁻¹ (the difference of radial velocities is ~ 45 km s⁻¹; Karachentsev et al. 2002), means that M81dwA could have passed close to HoII about 300 Myr ago, in good agreement with the beginning of the SFR enhancement. Both companion dwarfs also appear to have been experiencing higher star formation in the past few hundred million years than at older epochs (McQuinn et al. 2010; Warren et al. 2011).

However, tidal interaction is not the only process that can lead to enhanced star formation. In fact, hydrodynamical and N-body simulations of the interaction between the hot IGM and the ISM of a galaxy have shown that ram pressure can also result in increased star formation in the inner regions. The shockwaves resulting from the gas collision can increase significantly the central gas surface density and lead to the collapse of molecular clouds, thus enhancing the star formation rate (Quilis, Moore, & Bower 2000; Schulz & Struck 2001; Vollmer et al. 2001; Marcolini, Brighenti, & D'Ercole 2003). The fact that the spatial distribution of young stars closely follows that of the H_I contours strongly supports this interpretation. Such an enhancement of the star formation as a consequence of the interaction between ISM and IGM has also been observed in various galaxies as asymmetric H α enhancements, usually located along the leading edge of the galaxy disc (e.g. Koopmann & Kenney 2004; Crowl et al. 2005).

Therefore, while the morphology of the H_I cloud and the observed enhancement of the recent star formation rate cannot help discriminate between the phenomena at play, the regular circular distribution of the intermediate-age and old stars, the regular rotation of the H_I arms, the undisturbed H_I distribution of the two nearest dwarf companions and the lack of H_I bridges/filaments between them and HoII (Bureau et al. 2004; Chynoweth et al. 2009; Ott et al. 2012), all support the ram pressure stripping scenario. In addition, we do not find a stellar counterpart to the H_I cloud beyond $R \sim 7'$ where it becomes distorted and forms arms/tails, whereas tidal forces would affect gas and stars equally. Therefore, our data strongly suggest that ram pressure stripping is the main process responsible for the swept-back appearance of the H_I cloud.

7 SUMMARY AND CONCLUSIONS

We have carried out a wide-field survey of the M81 group dwarf galaxy Holmberg II based on deep Subaru/Suprime-Cam imaging in V and I . These observations cover the whole

extent of the galaxy, including the vast H_I cloud, and allow us to perform photometry of individual stars down to $I \sim 25.2$, i.e. about 1.5 mag below the tip of the RGB.

The deep CMDs reveal the presence of stellar populations of all ages, from a few Myr old (MS+BSG, RSG) to several Gyr old (RGB). While in most dwarf galaxies in the Local Universe the younger stars are found to be more centrally concentrated than the older populations (e.g. Zhang et al. 2012), we find that in HoII the old RGB stars are significantly more concentrated than the young MS+BSG stars. Indeed, we find that the exponential scalelength for the young MS+BSG population is much larger than that of the RGB component ($2.8' \pm 0.4'$ vs. $0.76' \pm 0.04'$, respectively). We speculate that the shockwave due to ram pressure increased the gas density in the central part of the H_I cloud and triggered star formation on large scales.

Our Subaru data enable us to construct a composite surface brightness profile for HoII by combining diffuse light in the central region with star counts at large radii. This profile is one of the deepest yet published for any galaxy, extending from the centre out to $R \sim 7'$ where $\mu_V = 32$ mag arcsec⁻². Fitting an exponential profile to the outer regions gives a (projected) scalelength of $0.70' \pm 0.01'$, corresponding to 0.69 ± 0.01 kpc at the distance of HoII.

Finally, we discuss the properties of the resolved stellar populations in the context of the morphology of the large H_I cloud in order to understand the origin of its swept-back, cometary appearance. Previous studies based on diffuse optical light or 21 cm data could not definitively determine whether the cloud shape was due to ram pressure from a hot IGM or to a tidal interaction with a nearby companion galaxy. Our deep photometry shows that the intermediate-age and old stars have a regular circular distribution and show no sign of tidal tails/streams. In addition, we find that there are very few, if any, HoII stars beyond $R \sim 7'$ where the H_I becomes distorted. Since tidal forces would affect gas and stars equally, our data strongly suggest that the spectacular morphology of the H_I cloud is due to ram pressure. The detection of significant amount of diffuse hot gas in the vicinity of HoII would further verify this.

ACKNOWLEDGMENTS

We are very grateful to the anonymous referee for a prompt report that helped us improve the manuscript, and would like to thank M. Bureau for providing the H_I density map of HoII. Support for this work was provided by a rolling grant from the Science and Technology Facilities Council. We acknowledge the usage of the HyperLeda database (<http://leda.univ-lyon1.fr>). This research has made use of THINGS, 'The H_I Nearby Galaxy Survey' (Walter et al. 2008), and the NASA/IPAC Infrared Science Archive, which is operated by the Jet Propulsion Laboratory, California Institute of Technology, under contract with the National Aeronautics and Space Administration.

REFERENCES

Barker M. K., Ferguson A. M. N., Irwin M., Arimoto N., Jablonka P., 2009, AJ, 138, 1469

Barker M. K., Ferguson A. M. N., Irwin M. J., Arimoto N., Jablonka P., 2012, MNRAS, 419, 1489

Bastian N., et al., 2011, MNRAS, 412, 1539

Bernard E. J., et al., 2012, MNRAS, 420, 2625

Bureau M., Carignan C., 2002, AJ, 123, 1316

Bureau M., Walter F., van Gorkom J., Carignan C., 2004, in Duc P.-A., Braine J., and Brinks E., eds, IAU Symposium Vol. 217, Recycling Intergalactic and Interstellar Matter, San Francisco: Astronomical Society of the Pacific, p. 452

Chung A., van Gorkom J. H., Kenney J. D. P., Vollmer B., 2007, ApJ, 659, L115

Chynoweth K. M., Langston G. I., Holley-Bockelmann K., Lockman F. J., 2009, AJ, 138, 287

Cignoni M., Cole A. A., Tosi M., Gallagher J. S., Sabbi E., Anderson J., Grebel E. K., Nota A., 2012, ApJ, 754, 130

Coleman M. G., Da Costa G. S., Bland-Hawthorn J., Freeman K. C., 2005, AJ, 129, 1443

Condon J. J., 1983, ApJS, 53, 459

Crowl H. H., Kenney J. D. P., van Gorkom J. H., Vollmer B., 2005, AJ, 130, 65

Cutri R. M., et al., 2003, 2MASS All Sky Catalog of Point Sources, p. 2246

Dalcanton J. J., et al., 2009, ApJS, 183, 67

Dalcanton J. J., et al., 2012, ApJS, 198, 6

de Blok W. J. G., Walter F., 2006, AJ, 131, 343

de Blok W. J. G., Walter F., Brinks E., Trachternach C., Oh S.-H., Kennicutt R. C., Jr., 2008, AJ, 136, 2648

Dobbs C. L., Theis C., Pringle J. E., Bate M. R., 2010, MNRAS, 403, 625

Elson R. A. W., Fall S. M., Freeman K. C., 1987, ApJ, 323, 54

Gavazzi G., Contursi A., Carrasco L., Boselli A., Kennicutt R., Scodéglio M., Jaffe W., 1995, A&A, 304, 325

Gentile G., Angus G. W., Famaey B., Oh S.-H., de Blok W. J. G., 2012, A&A, 543, A47

Greisen E. W., Calabretta M. R., 2002, A&A, 395, 1061

Hidalgo S. L., Aparicio A., Martínez-Delgado D., Gallart C., 2009, ApJ, 705, 704

Holmberg E., 1950, MeLu2, 128, 1

Irwin M. J., 1985, MNRAS, 214, 575

Irwin M. J., 1997, in Rodriguez Espinosa J. M., Herrero A., Sánchez F., eds, Instrumentation for Large Telescopes, Cambridge: Cambridge Univ. Press, p. 35

Irwin M., Lewis J., 2001, NewAR, 45, 105

Irwin M. J., et al., 2004, SPIE, 5493, 411

Karachentsev I. D., et al., 2002, A&A, 383, 125

Kenney J. D. P., van Gorkom J. H., Vollmer B., 2004, AJ, 127, 3361

Kennicutt R. C., Jr., 1998, ApJ, 498, 541

Kennicutt R. C., Jr., Roettiger K. A., Keel W. C., van der Hulst J. M., Hummel E., 1987, AJ, 93, 1011

King I., 1962, AJ, 67, 471

Koopmann R. A., Kenney J. D. P., 2004, ApJ, 613, 866

Lasker B. M., et al., 2008, AJ, 136, 735

McConnachie A. W., Irwin M. J., Ibata R. A., Ferguson A. M. N., Lewis G. F., Tanvir N., 2003, MNRAS, 343, 1335

McConnachie A. W., Venn K. A., Irwin M. J., Young L. M., Geehan J. J., 2007, ApJ, 671, L33

McQuinn M. K. B. W., et al., 2010, ApJ, 724, 49

Mapelli M., Moore B., Bland-Hawthorn J., 2008, MNRAS, 388, 697

Marcolini A., Brighenti F., D'Ercole A., 2003, MNRAS, 345, 1329

Marigo P., Girardi L., Bressan A., Groenewegen M. A. T., Silva L., Granato G. L., 2008, A&A, 482, 883

Miyazaki S., et al., 2002, PASJ, 54, 833

Mulchaey J. S., Davis D. S., Mushotzky R. F., Burstein D., 1993, ApJ, 404, L9

Oh S.-H., de Blok W. J. G., Brinks E., Walter F., Kennicutt R. C., Jr., 2011, AJ, 141, 193

Ott J., et al., 2011, AJ, preprint (astro-ph/1208.3737)

Paturel G., Petit C., Prugniel P., Theureau G., Rousseau J., Brouty M., Dubois P., Cambrésy L., 2003, A&A, 412, 45

Plummer H. C., 1911, MNRAS, 71, 460

Quilis V., Moore B., Bower R., 2000, Sci, 288, 1617

Ryder S. D., Purcell G., Davis D., Andersen V., 1997, PASA, 14, 81

Ryś A., Grocholski A. J., van der Marel R. P., Aloisi A., Annibali F., 2011, A&A, 530, A23

Schlegel D. J., Finkbeiner D. P., Davis M., 1998, ApJ, 500, 525

Schulz S., Struck C., 2001, MNRAS, 328, 185

Stanimirović S., Staveley-Smith L., Jones P. A., 2004, ApJ, 604, 176

Stanimirović S., Staveley-Smith L., Dickey J. M., Sault R. J., Snowden S. L., 1999, MNRAS, 302, 417

Stetson P. B., 1993, in Butler C. J., Elliott I., eds, IAU Colloq. Vol. 136, Stellar Photometry – Current Techniques and Future Developments, Cambridge Univ. Press, Cambridge, p. 291

Stetson P. B., 1994, PASP, 106, 250

Stewart S. G., et al., 2000, ApJ, 529, 201

Stinson G. S., Dalcanton J. J., Quinn T., Gogarten S. M., Kaufmann T., Wadsley J., 2009, MNRAS, 395, 1455

Sun M., 2012, NJPh, 14, 045004

Swaters R. A., 1999, PhD Thesis, Rijksuniversiteit Groningen, <http://irs.ub.rug.nl/ppn/186373880>

Vollmer B., Cayatte V., Balkowski C., Duschl W. J., 2001, ApJ, 561, 708

Vollmer B., 2003, A&A, 398, 525

Walter F., et al., 2007, ApJ, 661, 102

Walter F., Brinks E., de Blok W. J. G., Bigiel F., Kennicutt R. C., Jr., Thornley M. D., Leroy A., 2008, AJ, 136, 2563

Warren S. R., et al., 2011, ApJ, 738, 10

Weisz D. R., Skillman E. D., Cannon J. M., Dolphin A. E., Kennicutt R. C., Jr., Lee J., Walter F., 2008, ApJ, 689, 160

Weisz D. R., Skillman E. D., Cannon J. M., Dolphin A. E., Kennicutt R. C., Jr., Lee J., Walter F., 2009, ApJ, 704, 1538

Weisz, D. R., Dalcanton, J. J., Williams, B. F., et al., 2011, ApJ, 739, 5

Westfall K. B., Majewski S. R., Ostheimer J. C., Frinchaboy P. M., Kunkel W. E., Patterson R. J., Link R., 2006, AJ, 131, 375

Zabludoff A. I., Mulchaey J. S., 1998, ApJ, 496, 39

Zhang H.-X., Hunter D. A., Elmegreen B. G., Gao Y., Schruba A., 2012, AJ, 143, 47